Supplement of Solid Earth, 11, 1475–1488, 2020
https://doi.org/10.5194/se-11-1475-2020-supplement

Solid Earth Open Access EGU

Supplement of

Quantifying the buffering of oceanic oxygen isotopes at ancient midocean ridges

Yoshiki Kanzaki

Correspondence to: Yoshiki Kanzaki (kanzakiy@ucr.edu)

S1. Two-dimensional distributions of solid-rock and porewater $\delta^{18}O$ with different spreading rates and ocean depths

Figs. S1 and S2 provide 2D distributions of solid-rock and porewater $\delta^{18}O$ with different spreading rates (1×10^{-2}, 9×10^{-2} and 30×10^{-2} m yr^{-1}) and ocean depths (1 and 5 km) considered for the Precambrian in Section 3.3.

S2. Comparison with more oceanic rock $\delta^{18}O$ datasets

The present model simulation is only compared with the Samail ophiolite in Oman in the main text. This is because the Samail ophiolite provides one of the most complete datasets and has a general feature of ophiolite/oceanic crust $\delta^{18}O$ signatures. Nonetheless, comparison with other datasets available in the literature is useful for further contemplating the validity of the model, especially regarding the effect of various spreading rate environments.

Oceanic rock $\delta^{18}O$ has been reported by Barrett and Friedrichsen (1982), Alt et al. (1986, 1995), Stakes (1991), Alt and Bach (2006) and Gao et al. (2012) for the modern ocean crust and by Gregory and Taylor (1981), Cocker et al. (1982), Elthon et al. (1984), Agrinier et al. (1988), Schiffman and Smith (1988), Vibetti et al. (1989), Lecuyer and Fourcade (1991), Bickle and Teagle (1992) and Muehlenbachs et al. (2003) for Phanerozoic ophiolites (Table S1). Note that Precambrian ophiolites are excluded here because seawater $\delta^{18}O$ could have been significantly different from the present-day value during the Precambrian (e.g., Galili et al., 2019; Johnson and Wing, 2020), and thus may not be as useful as Phanerozoic ophiolites for assessing the model's validity. Not all the rock data has explicit information regarding depths where interactions with porewater occurred. Nonetheless, a general oceanic crustal $\delta^{18}O$ profile can be constrained by assuming depth intervals of 0–0.5, 0.5–2 and 2–6 km for the pillow basalt, sheeted dike and gabbro sections, respectively, and utilizing the $\delta^{18}O$ values reported for the corresponding types of rocks by the above authors (shaded areas in Fig. S3). The data with explicit sample depth information (symbols in Fig. S3) is directly compared with the calculated solid-rock $\delta^{18}O$ at 30 km from the ridge axis in the simulations that assume a seawater $\delta^{18}O$ value of 0 ‰ and a spreading rate of 1×10^{-2}, 3×10^{-2} and 9×10^{-2} m yr^{-1} (dotted, solid and dashed curves, respectively, in Fig. S3). Note that alteration of oceanic crust is assumed to have insignificant influences on solid-rock $\delta^{18}O$ at > 30 km (or after 0.33 to 3 million years with the spreading rates assumed above) from the rock formation at the ridge axis, which is consistent with the observation that significant oxygen isotope exchange is limited within < 10 million years from the ridge axis (Muehlenbachs, 1979). A direct comparison is thus justifiable assuming that all observed $\delta^{18}O$ data is from rocks that are older than the time duration for significant oxygen isotope exchange (Table S1 and Section S6).

The modern oceanic rock $\delta^{18}O$ is limited to relatively shallow depths compared to ophiolite data. Available data for solid-rock $\delta^{18}O$ against depth in the modern ocean crust is reasonably

consistent with the simulations. Specifically, data for Hole 504B with intermediate spreading rate by Alt et al. (1995) (blue squares in Fig. S3) is consistent with the standard simulation (solid curve); data for Hole 735B with a slow spreading rate by Alt and Bach (2006) is scattered (cyan stars) but not inconsistent with the three simulations (it is difficult to determine which model reproduces the data best); and data for Site 1256 with a fast spreading rate (red crosses; Gao et al., 2012) is comparable to the simulation with a large spreading rate (dashed curves). Only notable difference is recognized with data by Barrett and Friedrichsen (1982) (purple circles), which can be explained by assuming a smaller permeability and/or slower kinetics for oxygen isotope exchange (see Sections S3 and S4).

Ophiolite data also generally follows the $\delta^{18}O$ trend simulated by the model: the Samail ophiolite (green X marks in Fig. S3) is consistent with the standard simulation, as described in the main text; and the Troodos ophiolite with a smaller spreading rate (pink diamonds; Table S1) is closer to the simulation results with a smaller spreading rate (dotted curves). Notably, however, Muehlenbachs et al. (2003) reported solid-rock $\delta^{18}O$ that is significantly smaller than predicted by the model for ophiolite complex formed during the Paleozoic (orange triangles). This may be attributable to the lower contemporaneous seawater $\delta^{18}O$ (as low as -5 ‰; Galili et al., 2019), as well as a smaller permeability and/or kinetic constant for oxygen isotope exchange (see the paragraph just above).

Overall, consistency between the present simulations and observations remains reasonably well even with larger datasets. Indeed, changes in solid-rock $\delta^{18}O$ with the spreading rate predicted by the present model are largely consistent with the observations. However, caution should be exercised because variations in permeability and kinetic constant for oxygen isotope exchange will significantly modify the simplified relationship between the spreading rate and oceanic rock $\delta^{18}O$ (Fig. S3). Nonetheless, general results and conclusions will not be affected even with variations in the permeability and kinetics of oxygen isotope exchange within plausible ranges, as described in the following sections (Sections S3 and S4).

S3. Sensitivity to permeability distribution

Permeability distribution significantly affects hydrothermal flow geometry and intensity and thus ^{18}O distributions within oceanic crust. However, as long as the model can reproduce modern observations with a certain permeability distribution, general conclusions given in the main text remain valid. To demonstrate this, here we consider three different permeability distributions: case 1, which assumes the standard parameterization for permeability (Section 2.1); case 2, which assumes a larger length scale (500 m) for an e-fold permeability decrease with otherwise the same parameterization as in case 1; and case 3, which assumes larger values for both the e-folding length scale (500 m) and the permeability at the crust/ocean interface ($10^{-11.3}$ m^2). Note that the permeability at the crust/ocean interface is comparable to fractured rock permeability ($\geq 10^{-12}$ m^2; Fisher, 1998) in all three cases. The permeability is largest in case 3

and decreases from case 3 to 1 at any depths (Fig. S4). Consistently, water exchange increases from case 1 to 3 (1.2×10^{13}, 4.9×10^{13} and 1.2×10^{14} kg yr^{-1} in cases 1–3, respectively) with relatively invariant total heat flux at 0.74×10^{12} W (Fig. S5). Despite the significant difference especially in the water exchange, simulated δ^{18}O distributions are largely consistent with observations in all three cases (Fig. S6). In any of the three cases, oceanic rocks are relatively insensitive to seawater δ^{18}O (Fig. S6). Correspondingly, seawater-δ^{18}O buffering is relatively weak (Fig. S7): -0.4×10^9, -0.7×10^9 and -0.7×10^9 mol yr^{-1} ‰$^{-1}$ in cases 1–3, respectively (cf. Fig. 6).

S4. Sensitivity to oxygen isotope exchange kinetics

Water-rock interactions in the field can be slower than those in the laboratory by a factor of up to 10^3 (e.g., Pačes, 1983; Yokoyama and Banfield, 2002; White and Brantley, 2003; Wallmann et al., 2008). Additionally, specific surface area of marine basalt has ∼one order of magnitude variability (Nielsen and Fisk, 2010). Accordingly, the rate constant at reference temperature (5 °C) for oxygen isotope exchange (denoted as $k_{\mathrm{ex}}^{\mathrm{ref}}$ here) in natual systems can be reduced compared to the laboratory value ($10^{-6.6}$–$10^{-7.2}$ mol^{-1} kg yr^{-1}; Section 2.2) by a factor of up to 10^4 (cf. Cathles, 1983). Hence, $k_{\mathrm{ex}}^{\mathrm{ref}}$ can be assumed to range from $10^{-10.5}$ to $10^{-6.5}$ mol^{-1} kg yr^{-1} and the geometric mean of this range (i.e., $10^{-8.5}$ mol^{-1} kg yr^{-1}) is adopted as the standard value in the present study.

The large uncertainty in $k_{\mathrm{ex}}^{\mathrm{ref}}$, however, does not affect the general results and conclusions in the main text. Additional numerical experiments with $k_{\mathrm{ex}}^{\mathrm{ref}}$ varied in the range of $10^{-10.5}$–$10^{-6.5}$ mol^{-1} kg yr^{-1} (Figs. S8 and S9) with otherwise the standard modern configuration show the buffering intensity ranging from -0.4×10^9 to -0.3×10^9 mol yr^{-1} ‰$^{-1}$ (i.e., slope in Fig. S9), which is not significantly different from that in the standard simulation (-0.4×10^9 mol yr^{-1} ‰$^{-1}$). The values of solid rock δ^{18}O show consistently limited sensitivity to seawater δ^{18}O, but the depth to which solid rock δ^{18}O can be affected by seawater δ^{18}O becomes deeper with a smaller kinetic constant (Fig. S8). The mechanisms to cause the partial decoupling of oceanic crust from seawater δ^{18}O, i.e., kinetic inhibition and ^{18}O supply via transported solid rocks (Section 3), thus operate over the wide range of $k_{\mathrm{ex}}^{\mathrm{ref}}$, but the kinetic inhibition plays more dominant role with a smaller $k_{\mathrm{ex}}^{\mathrm{ref}}$.

S5. Effects of off-axis hydrothermal fluid circulation

The numerical model presented in the main text is designed to simulate hydrothermal fluid circulation and oxygen isotopes relatively close to midocean ridges, not for off-axis simulations (Stein et al., 1995). This is reasonable given that oxygen isotopic composition of oceanic rocks is determined within less than 10 million years from the ridge axis (Muehlenbachs, 1979). Nonetheless, to evaluate the effects of off-axis hydrothermal fluid circulation on the oxygen-

isotope buffering across a wider oceanic crust, an additional experiment (referred to as "off-axis experiment 1") was conducted with a wider calculation domain, 300 km (cf. 30 km in the standard simulation), and imposing artificial pressures from overlying fictitious sediments to cause off-axis water flows (cf. Fisher and Becker, 2000). Additional pressures of 10 MPa (corresponding to overlying sediments with, e.g., ∼1200 m thickness assuming 2700 kg m^{-3} for sediment grain density and 0.5 for sediment porosity) are imposed upon 25 MPa of default hydrostatic pressure (with the crust/ocean interface at 2.5 km water depth) in regions of 30–50, 70–100, 125–150, 175–200, 225–250 and 275–300 km from the ridge axis. The larger pressures from thicker sediments imposed upon wider distance-intervals than inferred from Fisher and Becker (2000) were necessary for the numerical stability in the wider calculation domain with limited resolution. Resulting total water exchange is 5.3×10^{15} kg yr^{-1}, which agrees with the estimated range (4×10^{14}–8×10^{15} kg yr^{-1}) for low temperature hydrothermal fluid flux (Elderfield and Schultz, 1996; Coogan and Gillis, 2013). However, cumulative heat flux in off-axis experiment 1 is 0.75×10^{12} W, smaller than the observation within 9 million years (corresponding to 270 km with 3×10^{-2} m yr^{-1} spreading rate) from the ridge axis, $3.8(\pm 2.1) \times 10^{12}$ W (Stein and Stein, 1994) (Fig. S10). To consider a system with a more heat flux closer to the observation average, another experiment (referred to as "off-axis experiment 2") was performed assuming 400 °C at the bottom of the wider calculation domain (cf. Iyer et al., 2010) with the same artificial pressures from overlying fictitious sediments as those in off-axis experiment 1. Off-axis experiment 2 yields 3.5×10^{12} W of cumulative heat flux and 5.6×10^{14} kg yr^{-1} of total water exchange, both of which are consistent with the observations (Stein and Stein, 1994; Elderfield and Schultz, 1996; Coogan and Gillis, 2013) (Fig. S10).

Oxygen isotope behaviors in the off-axis experiments are similar to those described in the main text (Figs. S11–S14). The buffering intensity (i.e., slope in Fig. S14) is -0.5×10^9 and -0.4×10^9 mol yr^{-1} $‰^{-1}$ in off-axis experiments 1 and 2, respectively, not so different from the standard simulation without off-axis water flows (Fig. S14). Solid rock $\delta^{18}O$ profiles at 300 km (or 10 Myr) show relative insensitivity to seawater $\delta^{18}O$, as observed in the standard case. The only notable difference from the standard case is that low-temperature isotope exchange reactions are enhanced relative to high-temperature reactions in the two off-axis experiments (Figs. S11–S14), which can be attributed to the assumed long time duration (i.e., 10 million years) for oxygen isotope exchange. Once a possible mechanism to cause the apparent cessation of effective oxygen isotope exchange (Muehlenbachs, 1979) is further implemented, however, the enhancement of low temperature alteration can no longer be observed (see Section S6 for the details). In any case, the results and conclusions given in the main text are valid whether or not off-axis water flows are included as revealed by the two experiments in this section.

S6. Time duration for oxygen isotope exchange during oceanic crust alteration

It has been observed that oceanic crust alteration has limited effects on oxygen isotope exchange between bulk rock and porewater after < 10 million years from the rock formation at midocean ridges (Muehlenbachs, 1979) as described in Sections 2, S2 and S5. The time duration during which oxygen isotopes exchange significantly occurs has an uncertainty because the cause of the apparent cessation of the reaction is not fully understood. One possible explanation can be a decline in reaction kinetics with age, which has been suggested to be caused by changes in fluid residence time (and thus porewater chemistry) and reactive surface area (e.g., White and Brantley, 2003; Maher et al., 2009). As described in Section S4, a water-rock interaction in the field can be slower than that in the laboratory by a factor of up to 10^3, and this kinetic discrepancy has been suggested to become larger for a rock of an older age (e.g., White and Brantley, 2003; Maher et al., 2004). To discuss the plausibility of assumed time duration for the present model (e.g., 1 million years in the standard simulation), we adopt the suggested age dependence of reaction kinetics based on laboratory experiments and field observations and evaluate when oxygen isotopes are no longer effectively exchanged between oceanic rocks and porewater.

Based on the summarized experimental and field data for mineral dissolution by Maher et al. (2004), one can assume that laboratory data can be applied to a rock that has reacted with porewater for $< 10^3$ years and then the reaction rate diminishes with age reciprocally. Thus, in this section we adopt the following equation for $k_{\mathrm{ex}}^{\mathrm{ref}}$ (the rate constant for oxygen isotope exchange at reference temperature 5 °C):

$$k_{\mathrm{ex}}^{\mathrm{ref}} = \begin{cases} 10^{-6.9} & (u \le 10^3) \\ 10^{-6.9}(u/10^3)^{-1} & (u > 10^3) \end{cases} \tag{S1}$$

where u denotes the age (yr) of rock at a given distance x from the ridge axis, i.e., $u = x/w$. In Eq. (S1), $10^{-6.9}$ mol^{-1} kg yr^{-1} is adopted as the laboratory value for $k_{\mathrm{ex}}^{\mathrm{ref}}$ (equivalent to the geometric mean of the range $10^{-6.6}$–$10^{-7.2}$ mol^{-1} kg yr^{-1} extrapolated from the experiments by Cole et al. (1987); Section 2.2). We use the flow and temperature field obtained for off-axis experiment 2 in Section S5 (Figs. S10c and d) because the calculation domain needs to be wide enough to evaluate the time duration for oxygen isotope exchange that can be as long as 10 million years (Muehlenbachs, 1979).

Oxygen isotope profiles in off-axis experiment 2 with implementing Eq. (S1) instead of the standard constant value ($10^{-8.5}$) for $k_{\mathrm{ex}}^{\mathrm{ref}}$ show significant changes (e.g., > 2 ‰) with age only within the first ∼0.1–1 million years (or 3–30 km) from the ridge axis (Fig. S15; cf. Figs. S11–S13). Accordingly, the assumption of apparent cessation of effective oxygen isotope exchange at 30 km from the ridge axis is not unreasonable. In addition, oceanic rocks simulated in this section show the relatively small sensitivity to seawater δ^{18}O (Fig. S16) and correspondingly

weak seawater-$\delta^{18}O$ buffering capacity (-0.5×10^9 mol yr^{-1} ‰$^{-1}$; cf. -0.4×10^9 mol yr^{-1} ‰$^{-1}$ in the standard case; Fig. S17). Therefore, the general results and conclusions presented in the main text will remain valid even in a wider calculation domain.

References

Abelson, M., Baer, G., and Agnon, A. (2001). Evidence from gabbro of the troodos ophiolite for lateral magma transport along a slow-spreading mid-ocean ridge. *Nature*, 409(6816):72–75.

Agrinier, P., Javoy, M., and Girardeau, J. (1988). Hydrothermal activity in a peculiar oceanic ridge: oxygen and hydrogen isotope evidence in the Xigaze ophiolite (Tibet, China). *Chemical Geology*, 71(4):313–335.

Alt, J. C. and Bach, W. (2006). Oxygen isotope composition of a section of lower oceanic crust, ODP Hole 735B. *Geochemistry, Geophysics, Geosystems*, 7(12).

Alt, J. C., Muehlenbachs, K., and Honnorez, J. (1986). An oxygen isotopic profile through the upper kilometer of the oceanic crust, DSDP Hole 504B. *Earth and Planetary Science Letters*, 80(3-4):217–229.

Alt, J. C., Zuleger, E., and Erzinger, J. (1995). Mineralogy and stable isotopic compositions of the hydrothermally altered lower sheeted dike complex, Hole 504B, Leg 140. In *Proceedings of the Ocean Drilling Program, Scientific Results*, volume 137, pages 155–166. Citeseer.

Barrett, T. J. and Friedrichsen, H. (1982). Strontium and oxygen isotopic composition of some basalts from Hole 504B, Costa Rica Rift, DSDP Legs 69 and 70. *Earth and Planetary Science Letters*, 60(1):27–38.

Bickle, M. J. and Teagle, D. A. H. (1992). Strontium alteration in the Troodos ophiolite: implications for fluid fluxes and geochemical transport in mid-ocean ridge hydrothermal systems. *Earth and Planetary Science Letters*, 113(1-2):219–237.

Cathles, L. (1983). An analysis of the hydrothermal system responsible for massive sulfide deposition in the Hokuroku Basin of Japan. *The Kuroko and Related Volcanogenic Massive Sulfide Deposits*, pages 439–487.

Cocker, J. D., Griffin, B. J., and Muehlenbachs, K. (1982). Oxygen and carbon isotope evidence for seawater-hydrothermal alteration of the Macquarie Island ophiolite. *Earth and Planetary Science Letters*, 61(1):112–122.

Cole, D. R., Mottl, M. J., and Ohmoto, H. (1987). Isotopic exchange in mineral-fluid systems. II. oxygen and hydrogen isotopic investigation of the experimental basalt-seawater system. *Geochimica et Cosmochimica Acta*, 51(6):1523–1538.

Coogan, L. A. and Gillis, K. M. (2013). Evidence that low-temperature oceanic hydrothermal systems play an important role in the silicate-carbonate weathering cycle and long-term climate regulation. *Geochemistry, Geophysics, Geosystems*, 14(6):1771–1786.

Elderfield, H. and Schultz, A. (1996). Mid-ocean ridge hydrothermal fluxes and the chemical composition of the ocean. *Annual Review of Earth and Planetary Sciences*, 24(1):191–224.

Elthon, D., Lawrence, J. R., Hanson, R. E., and Stern, C. (1984). Modelling of oxygen-isotope data from the Sarmiento ophiolite complex, Chile. *Geological Society, London, Special Publications*, 13(1):185–197.

Fisher, A. and Becker, K. (2000). Channelized fluid flow in oceanic crust reconciles heat-flow and permeability data. *Nature*, 403(6765):71.

Fisher, A. T. (1998). Permeability within basaltic oceanic crust. *Reviews of Geophysics*, 36(2):143–182.

Fonneland-Jorgensen, H., Furnes, H., Muehlenbachs, K., and Dilek, Y. (2005). Hydrothermal alteration and tectonic evolution of an intermediate-to fast-spreading back-arc oceanic crust: Late ordovician solund-stavfjord ophiolite, western norway. *Island Arc*, 14(4):517–541.

Galili, N., Shemesh, A., Yam, R., Brailovsky, I., Sela-Adler, M., Schuster, E. M., Collom, C., Bekker, A., Planavsky, N., Macdonald, F. A., Préat, A., Rudmin, M., Trela, W., Sturesson, U., Heikoop, J. M., Aurell, M., Ramajo, J., and Halevy, I. (2019). The geologic history of seawater oxygen isotopes from marine iron oxides. *Science*, 365(6452):469–473.

Gao, Y., Vils, F., Cooper, K. M., Banerjee, N., Harris, M., Hoefs, J., Teagle, D. A. H., Casey, J. F., Elliott, T., Laverne, C., Alt, J. C., and Muehlenbachs, K. (2012). Downhole variation of lithium and oxygen isotopic compositions of oceanic crust at east pacific rise, odp site 1256. *Geochemistry, Geophysics, Geosystems*, 13(10).

Gregory, R. T. and Taylor, Jr., H. P. (1981). An oxygen isotope profile in a section of cretaceous oceanic crust, Samail Ophiolite, Oman: Evidence for $\delta^{18}O$ buffering of the oceans by deep ($>$ 5 km) seawater-hydrothermal circulation at mid-ocean ridges. *Journal of Geophysical Research: Solid Earth*, 86(B4):2737–2755.

Iyer, K., Rüpke, L. H., and Morgan, J. P. (2010). Feedbacks between mantle hydration and hydrothermal convection at ocean spreading centers. *Earth and Planetary Science Letters*, 296(1-2):34–44.

Johnson, B. W. and Wing, B. A. (2020). Limited Archaean continental emergence reflected in an early Archaean ^{18}O-enriched ocean. *Nature Geoscience*, 13(3):243–248.

Lecuyer, C. and Fourcade, S. (1991). Oxygen isotope evidence for multi-stage hydrothermal alteration at a fossil slow-spreading center: The Silurian Trinity ophiolite (California, USA). *Chemical Geology: Isotope Geoscience section*, 87(3-4):231–246.

Maher, K., DePaolo, D. J., and Lin, J. C.-F. (2004). Rates of silicate dissolution in deep-sea sediment: In situ measurement using $^{234}U/^{238}U$ of pore fluids. *Geochimica et Cosmochimica Acta*, 68(22):4629–4648.

Maher, K., Steefel, C. I., White, A. F., and Stonestrom, D. A. (2009). The role of reaction affinity and secondary minerals in regulating chemical weathering rates at the Santa Cruz Soil Chronosequence, California. *Geochimica et Cosmochimica Acta*, 73(10):2804–2831.

Muehlenbachs, K. (1979). The alteration and aging of the basaltic layer of the seafloor: Oxygen isotope evidence from DSDP/IPOD Legs 51, 52, and 53. *Int. Repts. DSDP*, 51:1159–1167.

Muehlenbachs, K., Furnes, H., Fonneland, H. C., and Hellevang, B. (2003). Ophiolites as faithful records of the oxygen isotope ratio of ancient seawater: The Solund-Stavfjord Ophiolite Complex as a Late Ordovician example. *Geological Society, London, Special Publications*, 218(1):401–414.

Nielsen, M. E. and Fisk, M. R. (2010). Surface area measurements of marine basalts: implications for the subseafloor microbial biomass. *Geophysical Research Letters*, 37(15).

Pačes, T. (1983). Rate constants of dissolution derived from the measurements of mass balance in hydrological catchments. *Geochimica et Cosmochimica Acta*, 47(11):1855–1863.

Schiffman, P. and Smith, B. M. (1988). Petrology and oxygen isotope geochemistry of a fossil seawater hydrothermal system within the Solea graben, northern Troodos ophiolite, Cyprus. *Journal of Geophysical Research: Solid Earth*, 93(B5):4612–4624.

Stakes, D. S. (1991). Oxygen and hydrogen isotope composition of oceanic plutonic rocks: high-temperature deformation and metamorphism of oceanic layer 3. In *Stable Isotope Geochemistry: A Tribute to Samuel Epstein*, pages 77–90.

Stein, C. A. and Stein, S. (1994). Constraints on hydrothermal heat flux through the oceanic lithosphere from global heat flow. *Journal of Geophysical Research: Solid Earth*, 99(B2):3081–3095.

Stein, C. A., Stein, S., and Pelayo, A. M. (1995). Heat flow and hydrothermal circulation. *Seafloor Hydrothermal Systems: Physical, Chemical, Biological, and Geological Interactions*, pages 425–445.

Vibetti, N. J., Kerrich, R., and Fyfe, W. S. (1989). Oxygen and carbon isotope studies of hydrothermal alteration in the Troodos ophiolite complex, Cyprus. *Cyprus Crustal Study Project: Initial Report, Hole CY*, 4:88–9.

Wallmann, K., Aloisi, G., Haeckel, M., Tishchenko, P., Pavlova, G., Greinert, J., Kutterolf, S., and Eisenhauer, A. (2008). Silicate weathering in anoxic marine sediments. *Geochimica et Cosmochimica Acta*, 72(12):2895–2918.

White, A. F. and Brantley, S. L. (2003). The effect of time on the weathering of silicate minerals: why do weathering rates differ in the laboratory and field? *Chemical Geology*, 202(3-4):479–506.

Yamaoka, K., Ishikawa, T., Matsubaya, O., Ishiyama, D., Nagaishi, K., Hiroyasu, Y., Chiba, H., and Kawahata, H. (2012). Boron and oxygen isotope systematics for a complete section of oceanic crustal rocks in the Oman ophiolite. *Geochimica et Cosmochimica Acta*, 84:543–559.

Yokoyama, T. and Banfield, J. F. (2002). Direct determinations of the rates of rhyolite dissolution and clay formation over 52,000 years and comparison with laboratory measurements. *Geochimica et Cosmochimica Acta*, 66(15):2665–2681.

Table S1: Solid-rock $\delta^{18}O$ from the pillow basalt, sheeted dike and gabbro sections and spreading rate of the modern oceanic crust and Phanerozoic ophiolites.

Oceanic crust/ophiolite (age)	$\delta^{18}O$ (‰)			Spreading rate (cm yr^{-1})	Refs.[a]
	Basalt	Dike	Gabbro		
ODP Hole 504B (5.9 Ma)	5.8–12.7	3.6–6.5	na[b]	Medium (3.4)	1
ODP Hole 735B (∼12 Ma)	na[b]	na[b]	3.0–10.2	Slow (0.6–1)	2
ODP Site 1256 (15 Ma)	5.0–9.2	3.0–5.5	3.7–4.9	Fast (up to 20)	3
Macquaire Island (9–12 Ma)	5.8–9.7	4.0–8.8	2.6–5.7	Slow	4
Troodos (90–93 Ma)	9.2–14.4	2.2–13.6	1.1–10.4	Slow	5
Samail (100 Ma)	10.7–12.7	4.9–11.3	3.7–6.4	Fast	6
Xigaze (110–130 Ma)	9.6–15.6	7.2–9.4	4.8–11.5	Slow	7
Sarmiento (137–147 Ma)	6.4–10.4	3.0–8.1	2.6–7.6	na[b]	8
Trinity (420–440 Ma)	8.5–10.1	4.8–5.9	4.0–9.1	Slow	9
Solund-Stavfjord (443 Ma)	5.0–8.8	3.0–7.1	2.4–5.9	Medium–fast	10

[a] [1] Barrett and Friedrichsen (1982); Alt et al. (1986, 1995). [2] Stakes (1991); Alt and Bach (2006). [3] Gao et al. (2012). [4] Cocker et al. (1982). [5] Solid-rock $\delta^{18}O$ from Schiffman and Smith (1988); Vibetti et al. (1989); Bickle and Teagle (1992), spreading rate from Abelson et al. (2001). [6] Solid-rock $\delta^{18}O$ from Gregory and Taylor (1981), spreading rate from Yamaoka et al. (2012). [7] Agrinier et al. (1988). [8] Elthon et al. (1984). [9] Lecuyer and Fourcade (1991). [10] Solid-rock $\delta^{18}O$ from Muehlenbachs et al. (2003), spreading rate from Fonneland-Jorgensen et al. (2005).

[b] Not available.

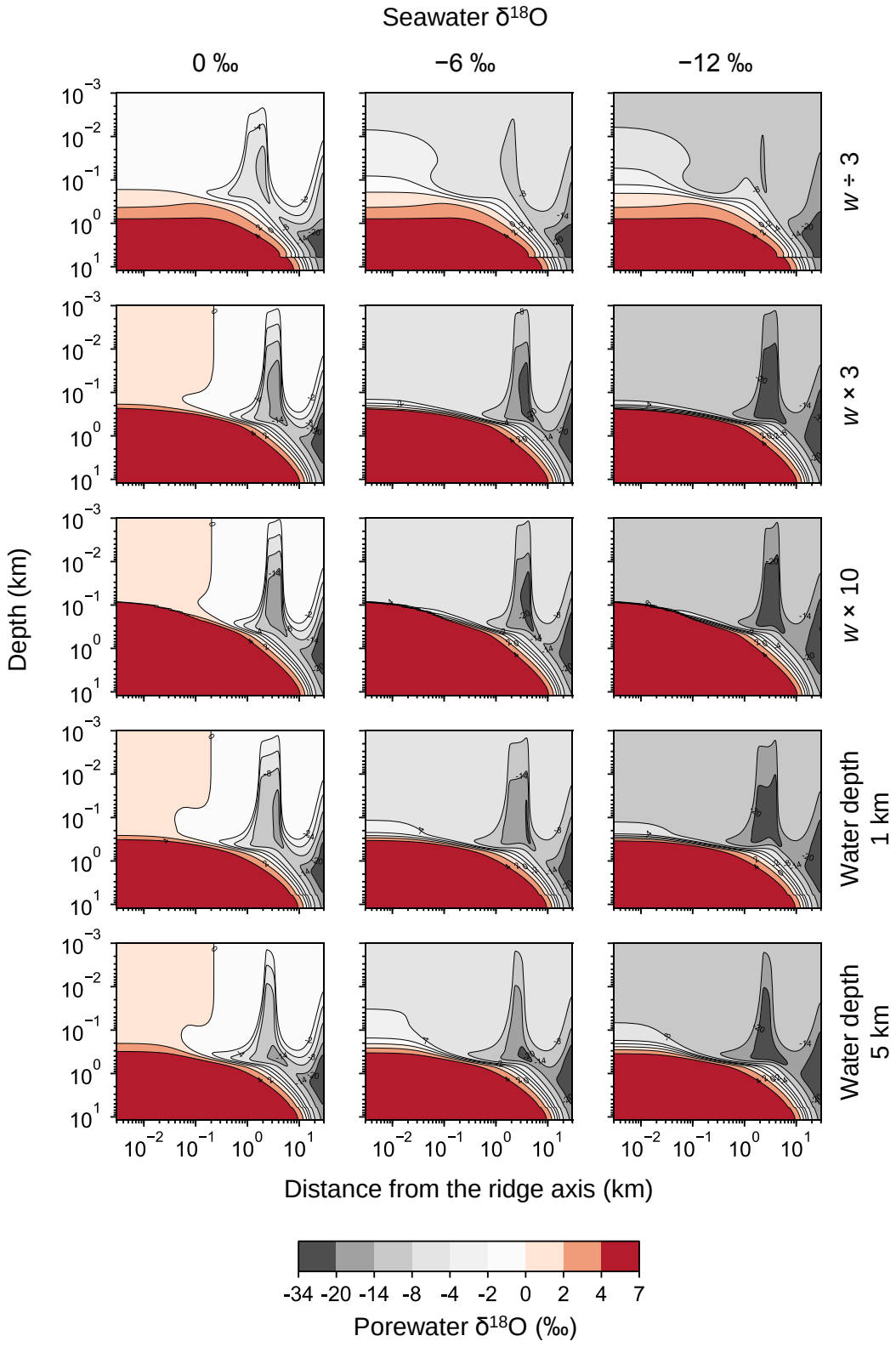

Figure S1: Two-dimensional distributions of porewater $\delta^{18}O$ at seawater $\delta^{18}O$ values of 0, −6 and −12 ‰ with different spreading rates and ocean depths. The panels in the first, second and third columns assume seawater $\delta^{18}O$ values of 0, −6 and −12 ‰, respectively, while those in the first, second, third, fourth and fifth rows adopt spreading rates of 1×10^{-2}, 9×10^{-2}, and 30×10^{-2} m yr^{-1} and ocean depths of 1 and 5 km, respectively, with other parameter values remaining the same as in the standard simulation (Sections 3.1 and 3.2).

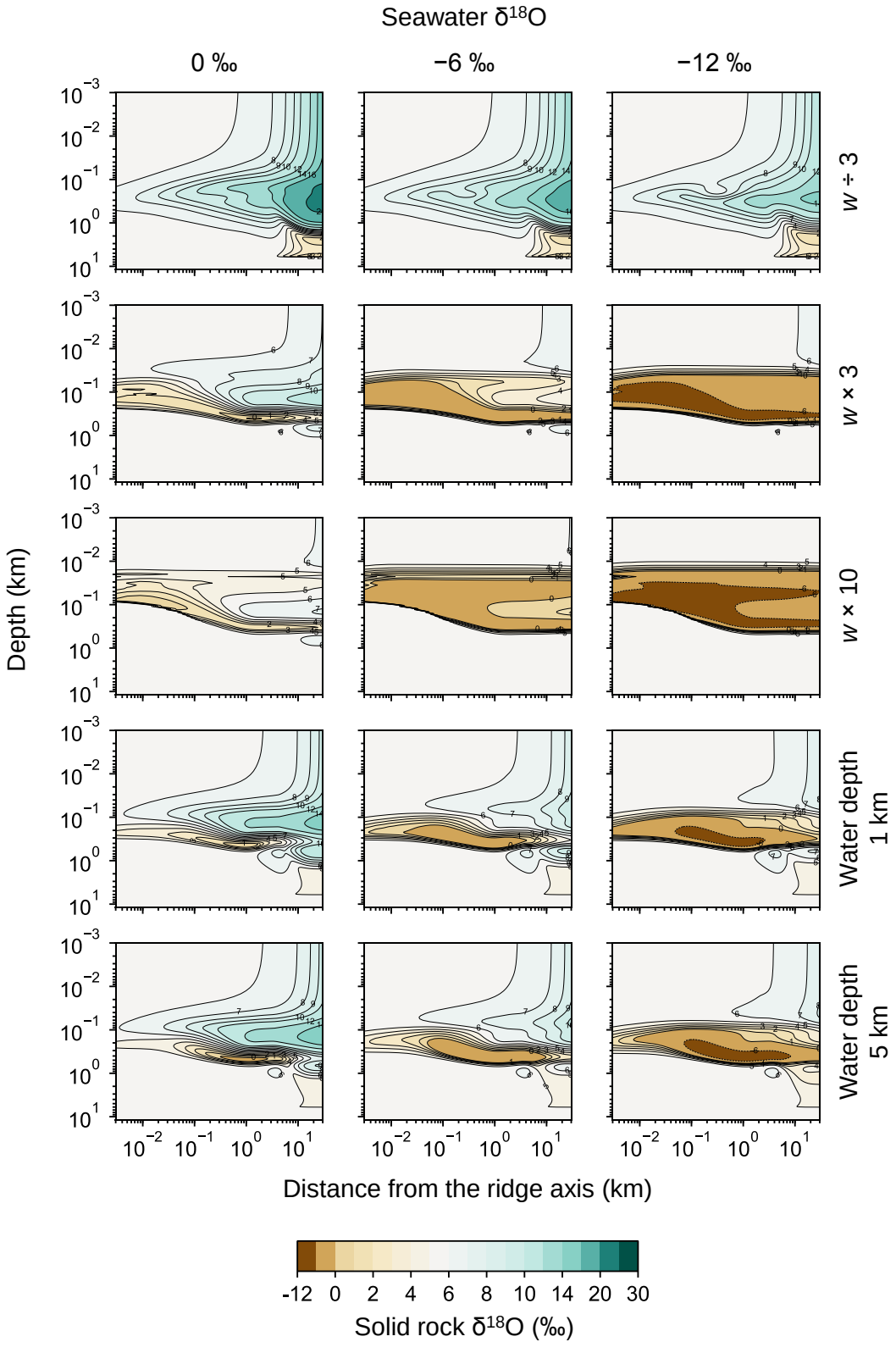

Figure S2: Two-dimensional distributions of solid rock δ^{18}O at seawater δ^{18}O values of 0, −6 and −12 ‰ with different spreading rates and ocean depths. The panels in the first, second and third columns assume seawater δ^{18}O values of 0, −6 and −12 ‰, respectively, while those in the first, second, third, fourth and fifth rows adopt spreading rates of 1×10^{-2}, 9×10^{-2}, and 30×10^{-2} m yr^{-1} and ocean depths of 1 and 5 km, respectively, with other parameter values remaining the same as in the standard simulation (Sections 3.1 and 3.2).

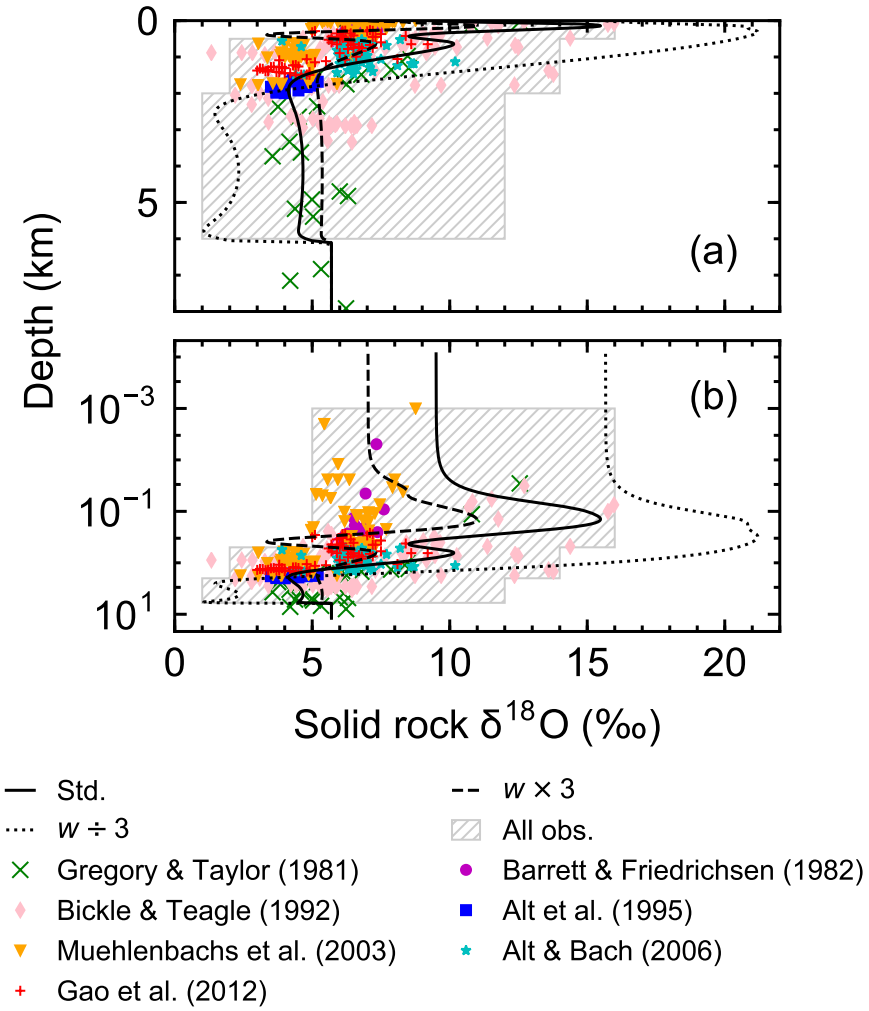

Figure S3: Comparison of observed and simulated oceanic crustal $\delta^{18}O$. The same data as in (a) is plotted in (b) except on the logarithmic depth scale. See Section S2 for the details of observed rock samples and simulations.

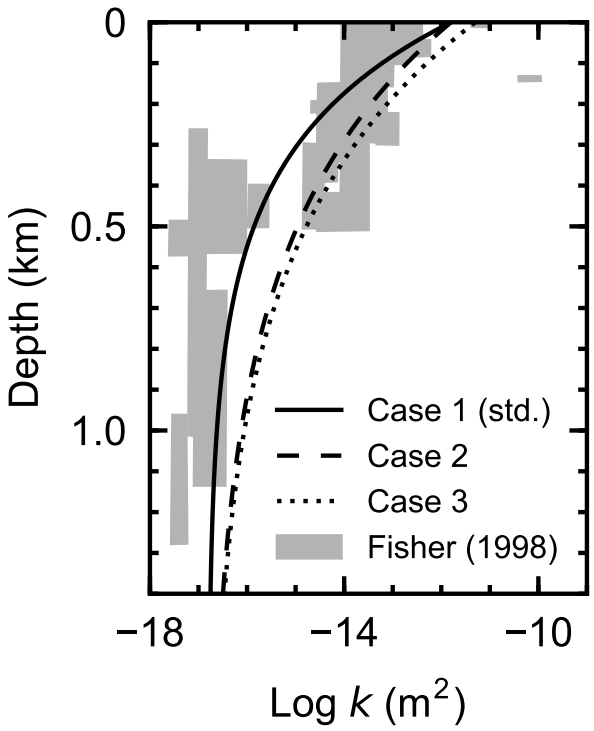

Figure S4: Permeability distributions assumed. See Section S3 for the details on cases 1–3. Gray regions show observed ranges (Fisher, 1998).

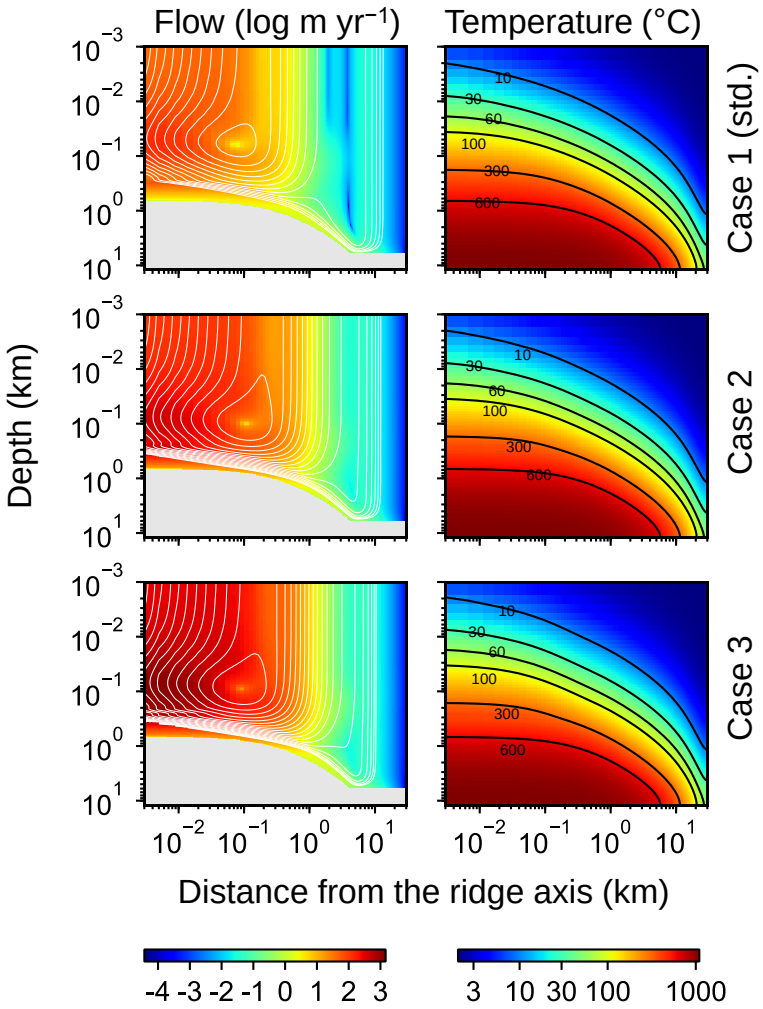

Figure S5: Two-dimensional distributions of hydrothermal fluid flow (left column) and temperature (right column) from simulations with different permeability distributions (cases 1–3 in Fig. S4; first, second and third rows, respectively). In left panels, logarithms of fluid velocity and mass-based stream lines are depicted and gray zones represent where rocks are impermeable below 6 km depth and/or with temperatures above the rock-cracking threshold (600 °C). See Section S3 for the details on cases 1–3.

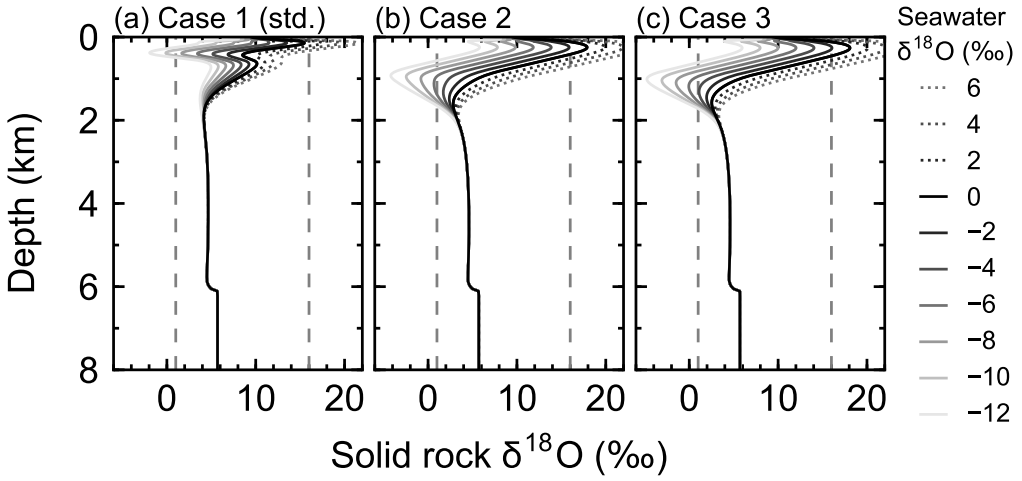

Figure S6: Solid rock $\delta^{18}O$ as function of depth at 30 km from the ridge axis at seawater $\delta^{18}O$ values of 6, 4, ..., −12 ‰ from simulations with different permeability distributions (cases 1–3 in Fig. S4; a–c, respectively). Dashed lines denote 1 and 16 ‰ between which observed $\delta^{18}O$ of ophiolites and/or oceanic crust ranges. See Section S3 for the details on cases 1–3.

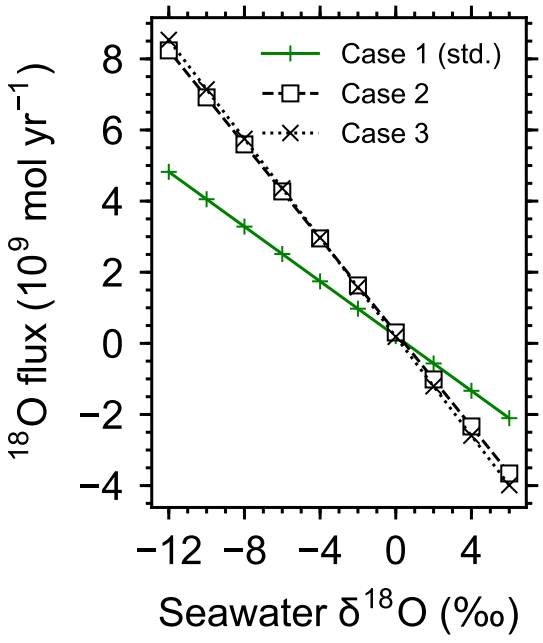

Figure S7: Net ^{18}O flux to the ocean from hydrothermal systems as function of seawater $\delta^{18}O$ from simulations with different permeability distributions (cases 1–3 in Fig. S4). See Section S3 for the details on cases 1–3.

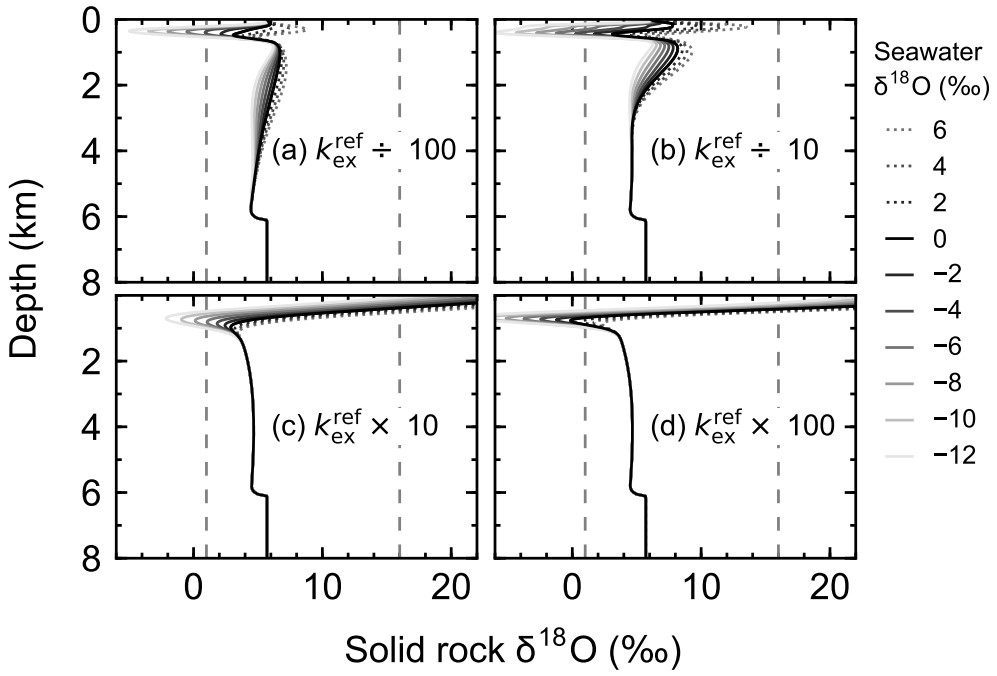

Figure S8: Solid rock $\delta^{18}O$ as function of depth at 30 km from the ridge axis at seawater $\delta^{18}O$ values of 6, 4, ..., −12 ‰ from simulations with different k_{ex}^{ref} values ($\log k_{ex}^{ref} = -10.5, -9.5, -7.5$ and -6.5 mol^{-1} kg yr^{-1} in a–d, respectively). See Section S4 for more details. Dashed lines denote 1 and 16 ‰ between which observed $\delta^{18}O$ of ophiolites and/or oceanic crust ranges.

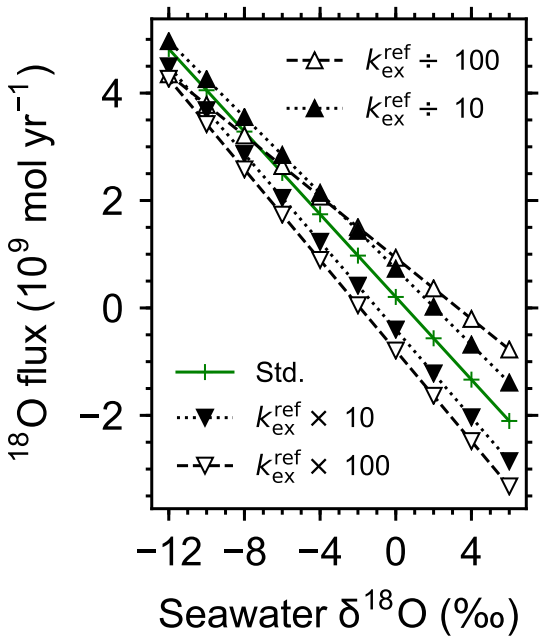

Figure S9: Net ^{18}O flux to the ocean from hydrothermal systems as function of seawater δ^{18}O from simulations with different k_{ex}^{ref} values ($\log k_{ex}^{ref} = -10.5, -9.5, -8.5, -7.5$ and -6.5 mol^{-1} kg yr^{-1}). See Section S4 for more details.

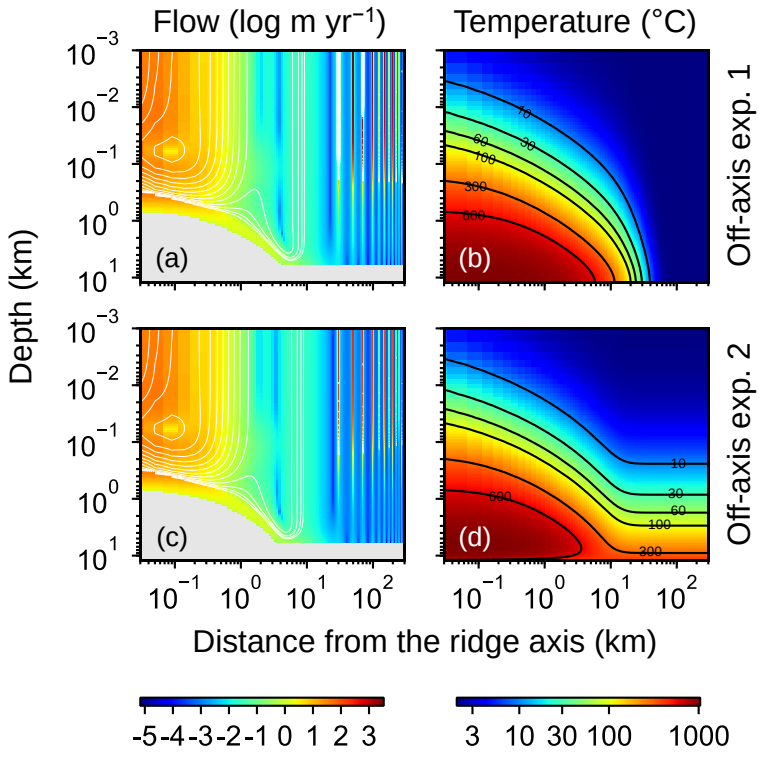

Figure S10: Two-dimensional distributions of hydrothermal fluid flow (a and c) and temperature (b and d) from off-axis experiments 1 (a and b) and 2 (c and d). In a and c, logarithms of fluid velocity and mass-based stream lines are depicted. See the caption of Fig. S5 for the explanation of gray zones in a and c. See Section S5 for the details on off-axis experiments 1 and 2.

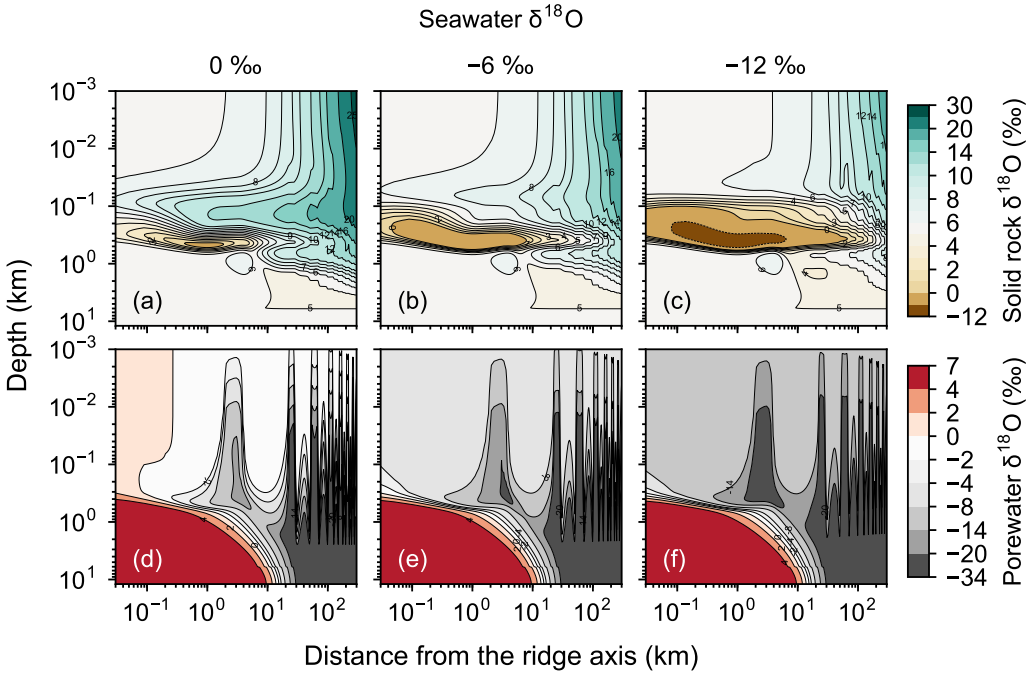

Figure S11: Two-dimensional distributions of solid-rock and porewater $\delta^{18}O$ (a–c and d–f, respectively) at seawater $\delta^{18}O$ values of 0, −6 and −12 ‰ (a and d, b and e, and c and f, respectively) from off-axis experiment 1. See Section S5 for the details on off-axis experiment 1.

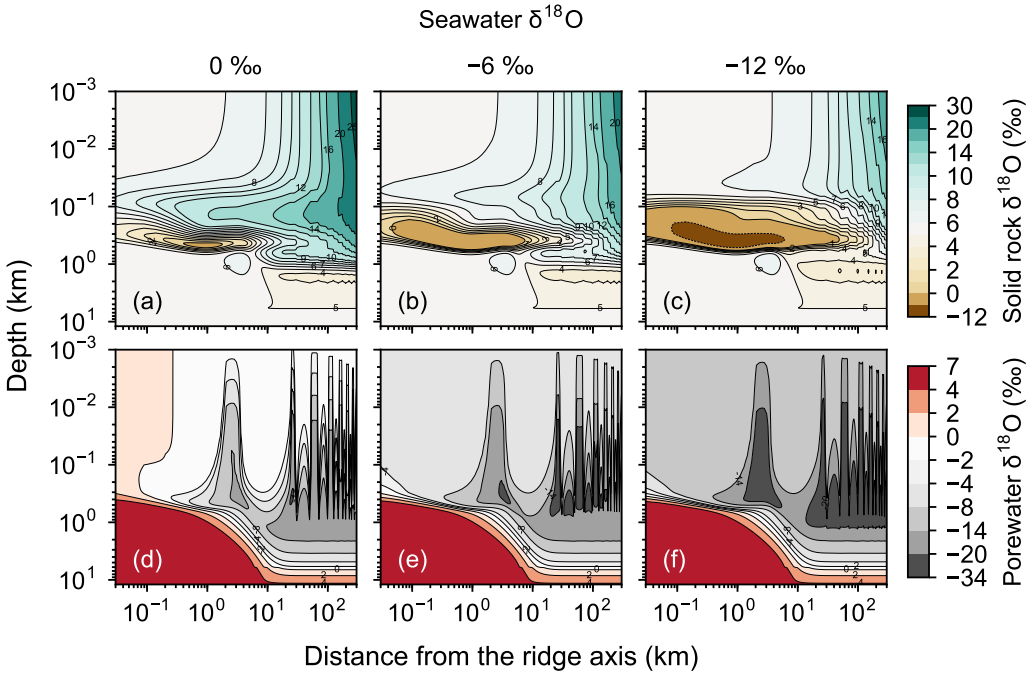

Figure S12: Two-dimensional distributions of solid-rock and porewater $\delta^{18}O$ (a–c and d–f, respectively) at seawater $\delta^{18}O$ values of 0, −6 and −12 ‰ (a and d, b and e, and c and f, respectively) from off-axis experiment 2. See Section S5 for the details on off-axis experiment 2.

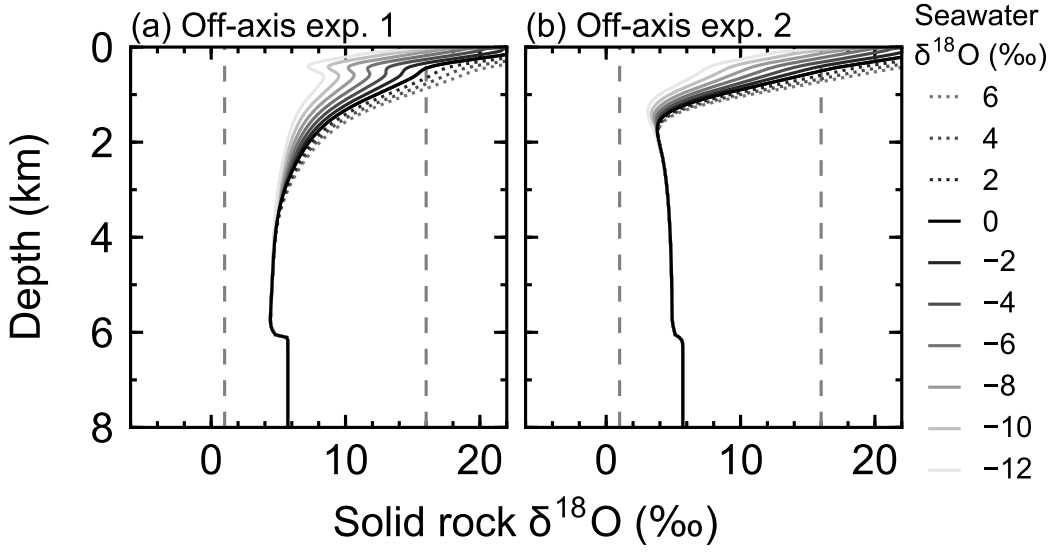

Figure S13: Solid rock $\delta^{18}O$ as function of depth at 300 km from the ridge axis at seawater $\delta^{18}O$ values of 6, 4, ..., −12 ‰ in off-axis experiments 1 and 2. See Section S5 for the details on off-axis experiments 1 and 2. Dashed lines denote 1 and 16 ‰ between which observed $\delta^{18}O$ of ophiolites and/or oceanic crust ranges.

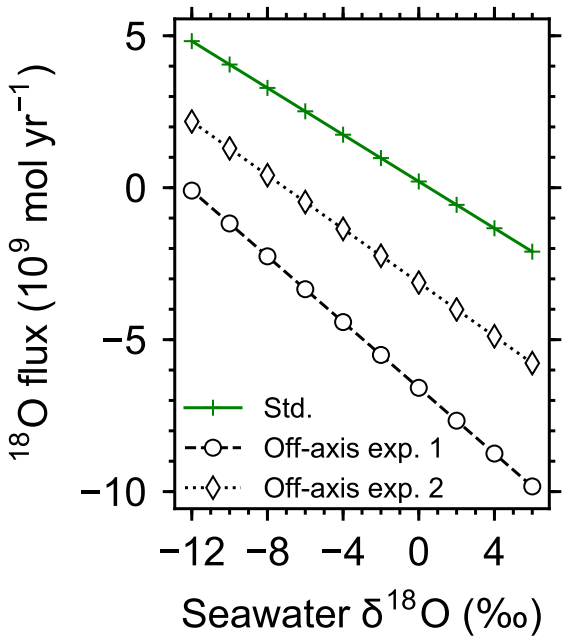

Figure S14: Net ^{18}O flux to the ocean from hydrothermal systems as function of seawater δ^{18}O from off-axis experiments 1 and 2 and the standard simulation. See Section S5 for the details on off-axis experiments 1 and 2.

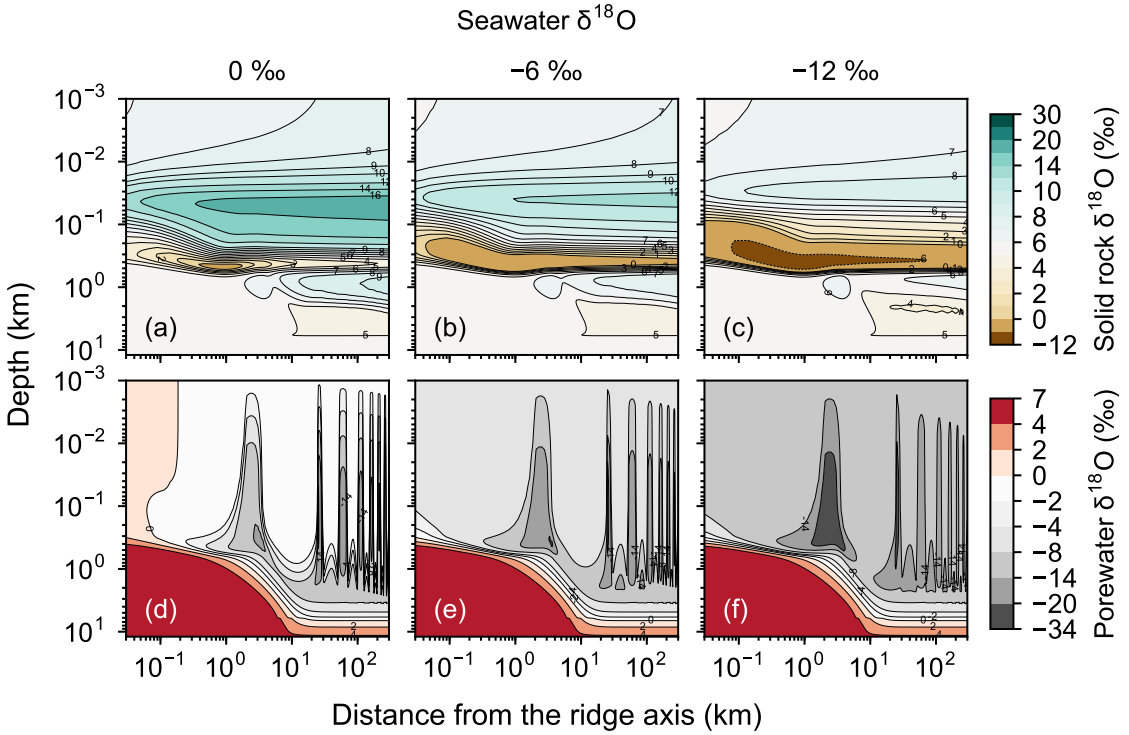

Figure S15: Two-dimensional distributions of solid-rock and porewater $\delta^{18}O$ (a–c and d–f, respectively) at seawater $\delta^{18}O$ values of 0, −6 and −12 ‰ (a and d, b and e, and c and f, respectively) from off-axis experiment 2 with implementing a decline in efficiency of oxygen isotope exchange with age (Eq. (S1), Section S6). See Section S5 for the details on off-axis experiment 2.

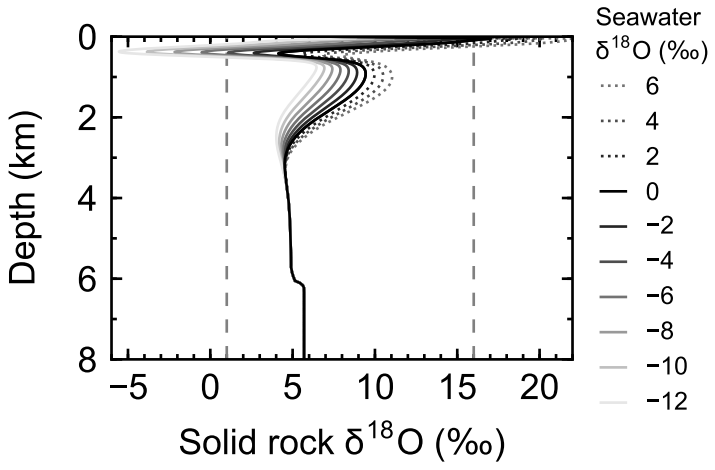

Figure S16: Solid rock $\delta^{18}O$ as function of depth at 300 km from the ridge axis at seawater $\delta^{18}O$ values of 6, 4, ..., −12 ‰ in off-axis experiment 2 with implementing a decline in efficiency of oxygen isotope exchange with age (Eq. (S1), Section S6). See Section S5 for the details on off-axis experiment 2. Dashed lines denote 1 and 16 ‰ between which observed $\delta^{18}O$ of ophiolites and/or oceanic crust ranges.

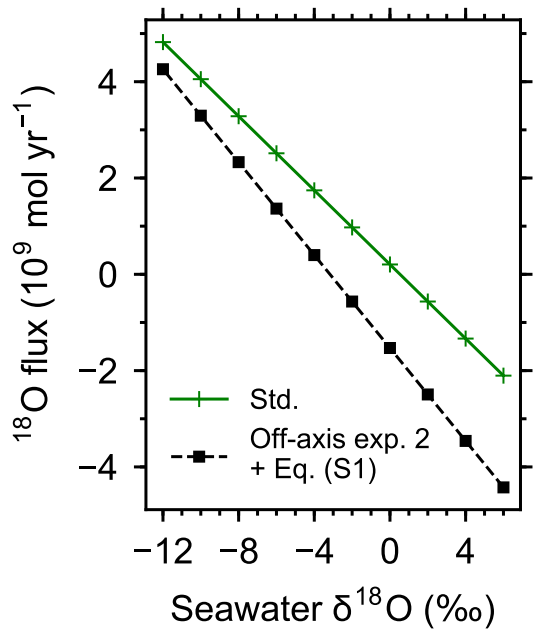

Figure S17: Net ^{18}O flux to the ocean from hydrothermal systems as function of seawater δ^{18}O from off-axis experiment 2 with implementing a decline in efficiency of oxygen isotope exchange with age (Eq. (S1), Section S6) and the standard simulation. See Section S5 for the details on off-axis experiment 2.